

Transfer Function Based Input Impedance Determination of Triple Active Bridge Converter

Jiajun Yang, Giampaolo Buticchi, Chunyang Gu, Sandro
Günter, Hao Yan, Pat Wheeler



**University of
Nottingham**
UK | CHINA | MALAYSIA

Faculty of Science and Engineering, University of Nottingham Ningbo China, 199 Taikang East Road, Ningbo, 315100, Zhejiang, China.

First published 2020

This work is made available under the terms of the Creative Commons Attribution 4.0 International License:

<http://creativecommons.org/licenses/by/4.0>

The work is licenced to the University of Nottingham Ningbo China under the Global University Publication Licence:

<https://www.nottingham.edu.cn/en/library/documents/research-support/global-university-publications-licence.pdf>



**University of
Nottingham**
UK | CHINA | MALAYSIA

Transfer Function Based Input Impedance Determination of Triple Active Bridge Converter

Jiajun Yang, Giampaolo Buticchi, Chunyang Gu, Sandro Güter, Hao Yan, Pat Wheeler

Key Laboratory of More Electric Aircraft Technology of Zhejiang Province

University of Nottingham Ningbo China

Ningbo, China

jiajun_yang@outlook.com

Abstract—The concept of multiport dc-dc converter was proposed to reduce the conversion stages of dc microgrid on more electric aircraft (MEA). The structure of multiport dc-dc converter is basically developed from the dual active bridge (DAB) converter because of its galvanic isolation and bidirectional power flow. A power electronics converter as a key element of the electrical power distribution system may cause stability issues. To address these challenges, the impedance characteristic of the multiport converter will be analyzed. In this paper, a transfer function based small signal model is developed and validated with a switching model, to figure out the characteristic of input impedance of triple active bridge (TAB) converter. Preliminary experimental results are presented to be as a support.

Keywords—dc-dc converter, input impedance, multiport, more electric aircraft.

I. INTRODUCTION

Nowadays, the electrification of transportation becomes an irresistible trend to cope with the lack of conventional energies and environmental deterioration. In the aspect of aerospace, the concept of all electric aircraft (AEA) which emphasizes using onboard electrical devices to power main engine and propulsion engine at startup, was considered by military aircraft engineers since World War II [1]. However, this thorough change of on-board devices will increase the unknown stability issues in aircraft while the gains cannot satisfy the conservative aerospace industry [2]. As a step-wise approach, the concept of more electric aircraft (MEA) which proposes to achieve electrification of subsystems on aircraft, is more preferred by aerospace industry and researchers. Compared to conventional aircraft, MEA has advantages of lower maintenance cost, lower weight and positive environmental impacts [3]. During the last several decades, significant progress has been achieved to move toward MEA. Many on-board devices which use hydraulic, mechanical and pneumatic power have been replaced by electrical devices [4].

As on-board electrical devices increase, the potential risks in power distribution are increasing as well. The aircraft can be regarded as an isolated system connected to generators and loads, and the distribution system can be regarded as an on-board microgrid [5]. To standardize different requirements according to the number of installed power electronics and the characteristics of the actuator, several different voltage standards containing both ac and dc levels for electrical system on large civilian aircraft are stated in [6]. Compared with ac microgrid,

dc microgrid (± 270 V dc bus and 28 V dc bus) is preferred by more researchers because of its lower current rating and fewer conversion stages, indicating higher efficiency [5],[7]. The structure of dc microgrid is shown in Fig. 1. A conventional dc microgrid consists of multiple dc-dc converters to achieve different dc voltage levels for individual use. Although this pattern allows the power to be transferred simultaneously, it has many conversion stages and communication devices between converters, resulting in complex structure and high cost. Based on this fact, multiport dc-dc converter was proposed in [8] to reduce the conversion stages. Moreover, droop control based hierarchical control proposed in [9] is deemed effective to cut down the communication devices in microgrid.

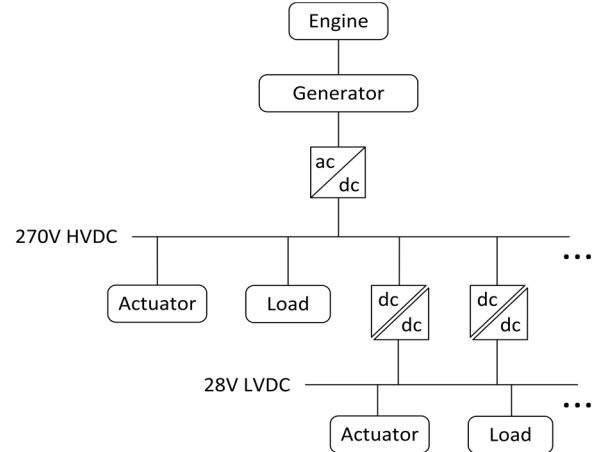


Fig. 1. dc microgrid on MEA

Considering the safety purpose, the dc-dc converter used for MEA must have the characteristic of galvanic isolation [10]. The most popular topology is dual active bridge (DAB) converter which is composed of two H-bridges and a high frequency (HF) transformer. With such a structure, bidirectional power flow can be easily achieved by means of control. Based on this topology, a triple active bridge (TAB) converter was proposed and verified in [11] and a quadruple active bridge (QAB) converter was proposed and verified in [12]. Although these multiport dc-dc converters are thought highly to replace general two-port dc-dc converters in the future, the stability of them needs to be assessed when they are interfaced to sources and loads in microgrid of MEA.

In this paper, the characteristic of the input impedance of TAB converter is investigated and validated. Section II presents

the structure and operating principle of TAB converter. Section III shows the transfer function based small signal model of TAB converter. Section IV gives the specifications for TAB converter. Section V investigates and validates the characteristic of input impedance of TAB converter by using both Matlab and PLECS. Section VI shows preliminary experimental results. Section VII draws the conclusion.

II. TRIPLE ACTIVE BRIDGE CONVERTER

Generally, the TAB converter can be used to interface multiple buses or as a storage management system. In this paper, the TAB converter is supposed to connect dc bus and resistive loads to facilitate the simulation and validation of model.

A. The structure

Fig. 2 shows basic structure of TAB converter.

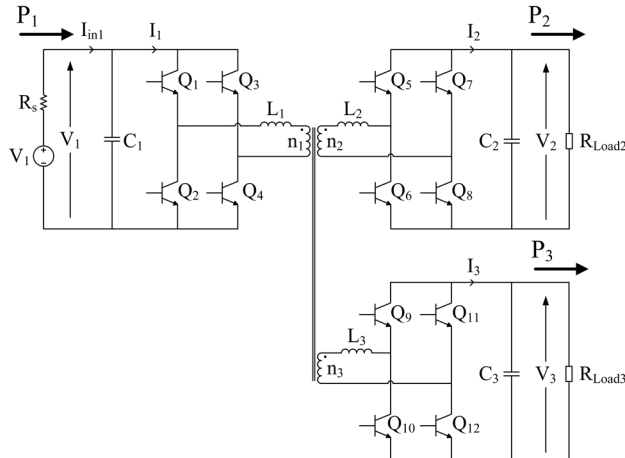


Fig. 2. The basic structure of TAB converter

As Fig. 2 shows, Port 1 is connected to dc bus, Port 2 and Port 3 are connected to resistive loads. By controlling the phase shift among the switching signals of all three ports, the power flow among three ports can be enabled. Also, lead and lag of switching signals will decide the direction of power flow. The individual power transferred between any two ports is given as

$$P_{ij} = \frac{V_i V_j}{2n_{ij} f_s L_{ij}} d_{ij} (1 - |d_{ij}|) \quad (2.1)$$

Where V_i is the voltage of Port i, V_j is the voltage of Port j, n_{ij} is the turn ratio between Port i and Port j, L_{ij} is the leakage inductance between Port i and Port j, d_{ij} is the phase shift ratio normalizing the phase shift angle to π . Hence, to obtain the real value of the leakage inductance in Equation (2.1), the proper transformer model needs to be figured out. Fig. 3 shows the transformer models of TAB converter, containing both star model and delta model.

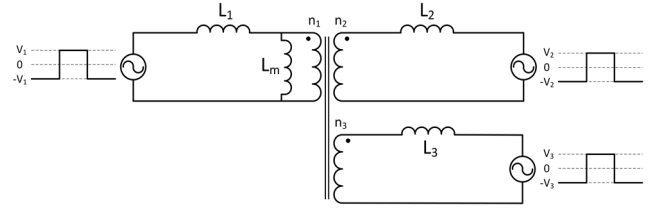
In Fig. 3(b) the star model, the inductance and voltage of Port 2 and Port 3 referred to Port 1 are calculated as:

$$L'_2 = \frac{n_1^2 L_2}{n_2^2}, \quad L'_3 = \frac{n_1^2 L_3}{n_3^2}, \quad V_2' = \frac{n_1 V_2}{n_2}, \quad V_3' = \frac{n_1 V_3}{n_3} \quad (2.2)$$

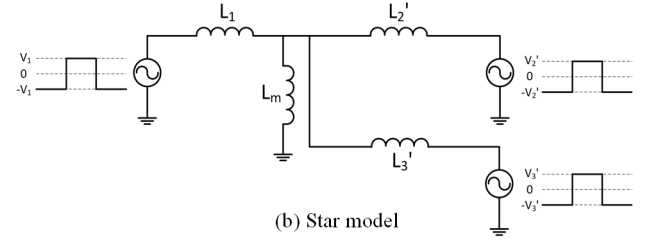
To be consistent with the inductance used in Equation (2.1), the delta model is adopted by calculating its leakage inductance. The

approach was introduced in [11]. Assuming the magnetizing inductance L_m is super large that can be regarded as open circuit, the inductance on each branch in Fig. 3(c) can be derived as

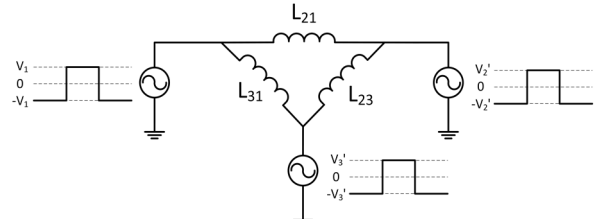
$$\begin{aligned} L_{21} &= \frac{\left[L_1 + \left(\frac{1}{L'_2} + \frac{1}{L'_3} \right)^{-1} \right] (L'_2 + L'_3)}{L'_3} = \frac{L_1 L'_2 + L_1 L'_3 + L'_2 L'_3}{L'_3} \\ L_{31} &= \frac{\left[L_1 + \left(\frac{1}{L'_2} + \frac{1}{L'_3} \right)^{-1} \right] (L'_2 + L'_3)}{L'_2} = \frac{L_1 L'_2 + L_1 L'_3 + L'_2 L'_3}{L'_2} \\ L_{23} &= \frac{\left[L'_3 + \left(\frac{1}{L_1} + \frac{1}{L'_2} \right)^{-1} \right] (L_1 + L'_2)}{L_1} = \frac{L_1 L'_2 + L_1 L'_3 + L'_2 L'_3}{L_1} \end{aligned} \quad (2.3)$$



(a) Simplified structure



(b) Star model



(c) Delta model

Fig. 3. The transformer model of TAB converter

B. Operating principle

The operating principle of TAB converter is similar to DAB converter. The switching signals and leakage inductance current are represented in Fig. 4. Considering the conservation of power, the port power P_1 , P_2 and P_3 designated in Fig. 2 satisfy the equation

$$P_1 = P_2 + P_3 \quad (2.4)$$

With the operating principle shown in Fig. 4, the individual power P_{21} , P_{31} and P_{23} can be used to present the port power P_1 , P_2 and P_3

$$P_1 = P_{21} + P_{31}, \quad P_2 = P_{21} + P_{23}, \quad P_3 = P_{31} - P_{23} \quad (2.5)$$

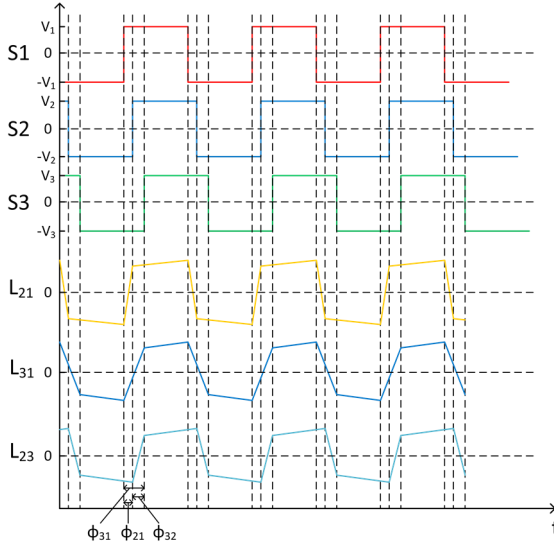


Fig. 4. The operating waveforms of TAB converter

Since Port 2 and Port 3 are supposed to connect the resistive loads, P_2 and P_3 cannot be negative. This can be concluded to the individual phase shift that two conditions will never happen in nearly linear operating region: (a) $d_{31} < d_{23}$ and (b) $d_{21} < d_{32}$. When $d_{31} = d_{23}$ or $d_{21} = d_{32}$, it means resistive load at Port 2 or Port 3 is disconnected.

III. TRANSFER FUNCTION BASED SMALL SIGNAL MODEL

State-space averaging and circuit averaging are two conventional techniques to obtain the small signal model of converter [13]. However, it becomes difficult to use these two techniques to model the converter including more components, such as DAB converter. In this section, an alternative technique is proposed, which uses the small signal equations derived from power equation, to acquire the small signal model of input impedance of TAB converter. Assume Port 1 as the driving point port, according to Equation (2.1) and (2.5), the current of each port can be obtained as

$$I_1 = \frac{V_2}{2n_{21}f_sL_{21}} d_{21}(1 - |d_{21}|) + \frac{V_3}{2n_{31}f_sL_{31}} d_{31}(1 - |d_{31}|) \quad (3.1)$$

$$I_2 = \frac{V_1}{2n_{21}f_sL_{21}} d_{21}(1 - |d_{21}|) + \frac{V_3}{2n_{23}f_sL_{23}} d_{23}(1 - |d_{23}|) \quad (3.2)$$

$$I_3 = \frac{V_1}{2n_{31}f_sL_{31}} d_{31}(1 - |d_{31}|) - \frac{V_2}{2n_{23}f_sL_{23}} d_{23}(1 - |d_{23}|) \quad (3.3)$$

where $n_{21} = \frac{n_2}{n_1}$, $n_{31} = \frac{n_3}{n_1}$, $n_{23} = \frac{n_2}{n_3}$.

Then the small signal equations can be obtained by deriving Equation (3.1) – (3.3) partially to voltage and phase shift ratio. In the calculation of the small signal equations, d_{23} is supposed to be substituted by $d_{21} - d_{31}$, since this substitution will simplify the equations and undermentioned transfer function block scheme largely. The small signal equations are derived and represented as Matrix (3.4) at the bottom side of this page. Based on this, a transfer function block scheme can be drawn as Fig. 5.

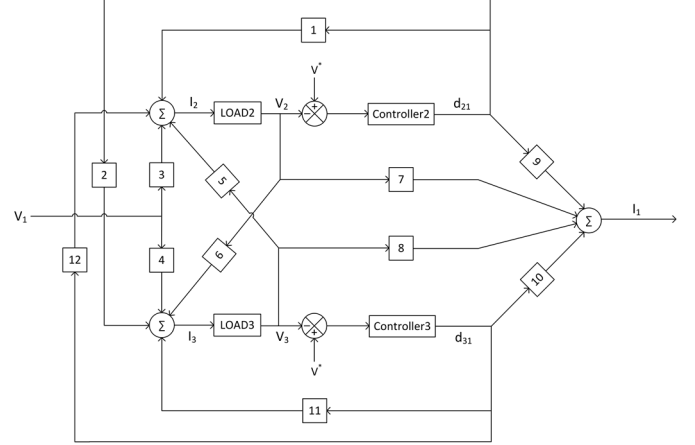


Fig. 5. The block scheme of TAB converter

In Fig. 5, there are totally twelve gain blocks 1-12 corresponding to the gains in Matrix (3.4) multiplied with a first-order transfer function which presents the time delay in both switches and controllers. The specific equations of these twelve blocks are depicted as

$$G_1 = \left[\frac{V_1}{2n_{21}f_sL_{21}}(1 - |2d_{21}|) + \frac{V_3}{2n_{23}f_sL_{23}}(1 - |2d_{21} - 2d_{31}|) \right] \times \frac{1}{ts + 1}$$

$$G_2 = -\frac{V_2}{2n_{23}f_sL_{23}}(1 - |2d_{21} - 2d_{31}|) \times \frac{1}{ts + 1}$$

$$G_3 = \frac{1}{2n_{21}f_sL_{21}} d_{21}(1 - |d_{21}|) \times \frac{1}{ts + 1}$$

$$G_4 = \frac{1}{2n_{31}f_sL_{31}} d_{31}(1 - |d_{31}|) \times \frac{1}{ts + 1}$$

$$G_5 = \frac{1}{2n_{23}f_sL_{23}} (d_{21} - d_{31})(1 - |d_{21} - d_{31}|) \times \frac{1}{ts + 1}$$

$$G_6 = -\frac{1}{2n_{23}f_sL_{23}} (d_{21} - d_{31})(1 - |d_{21} - d_{31}|) \times \frac{1}{ts + 1}$$

$$G_7 = \frac{1}{2n_{21}f_sL_{21}} d_{21}(1 - |d_{21}|) \times \frac{1}{ts + 1}$$

$$G_8 = \frac{1}{2n_{31}f_sL_{31}} d_{31}(1 - |d_{31}|) \times \frac{1}{ts + 1}$$

$$\begin{aligned} \begin{pmatrix} I_1 \\ I_2 \\ I_3 \end{pmatrix} = & \begin{pmatrix} 0 & \frac{1}{2n_{21}f_sL_{21}} d_{21}(1 - |d_{21}|) & \frac{1}{2n_{31}f_sL_{31}} d_{31}(1 - |d_{31}|) & \frac{V_2}{2n_{21}f_sL_{21}}(1 - |2d_{21}|) & \frac{V_3}{2n_{31}f_sL_{31}}(1 - |2d_{31}|) \\ \frac{1}{2n_{21}f_sL_{21}} d_{21}(1 - |d_{21}|) & 0 & \frac{1}{2n_{23}f_sL_{23}} (d_{21} - d_{31})(1 - |d_{21} - d_{31}|) & \frac{V_1}{2n_{21}f_sL_{21}}(1 - |2d_{21}|) + \frac{V_3}{2n_{23}f_sL_{23}}(1 - |2d_{21} - 2d_{31}|) & \frac{V_3}{2n_{23}f_sL_{23}}(-1 + |2d_{21} - 2d_{31}|) \\ \frac{1}{2n_{31}f_sL_{31}} d_{31}(1 - |d_{31}|) & -\frac{1}{2n_{23}f_sL_{23}} (d_{21} - d_{31})(1 - |d_{21} - d_{31}|) & 0 & -\frac{V_2}{2n_{23}f_sL_{23}}(1 - |2d_{21} - 2d_{31}|) & \frac{V_1}{2n_{31}f_sL_{31}}(1 - |2d_{31}|) - \frac{V_2}{2n_{23}f_sL_{23}}(-1 + |2d_{21} - 2d_{31}|) \end{pmatrix} \begin{pmatrix} \hat{P}_1 \\ \hat{P}_2 \\ \hat{P}_3 \\ d^{21} \\ d^{31} \end{pmatrix} \end{aligned} \quad (3.4)$$

$$\begin{aligned}
G_9 &= \frac{V_2}{2n_{21}f_sL_{21}}(1 - |2d_{21}|) \times \frac{1}{ts + 1} \\
G_{10} &= \frac{V_3}{2n_{31}f_sL_{31}}(1 - |2d_{31}|) \times \frac{1}{ts + 1} \\
G_{11} &= \left[\frac{V_1}{2n_{31}f_sL_{31}}(1 - |2d_{31}|) - \frac{V_2}{2n_{23}f_sL_{23}}(-1 + |2d_{21} - 2d_{31}|) \right] \times \frac{1}{ts + 1} \\
G_{12} &= \frac{V_3}{2n_{23}f_sL_{23}}(-1 + |2d_{21} - 2d_{31}|) \times \frac{1}{ts + 1}
\end{aligned} \tag{3.5}$$

where τ is one switching period of TAB converter.

By simplifying the block scheme, the input admittance of TAB converter can be derived as

$$Y_i = \frac{I_i}{V_i} = \frac{-(f+gd)}{e+cg} \left(G_9 + \left(\frac{G_7}{-ctrl_2} \right) \right) + \frac{-(f+be)}{ae+g} \left(G_{10} + \left(\frac{G_8}{-ctrl_3} \right) \right) \tag{3.6}$$

The coefficients are as follows

$$\begin{aligned}
a &= \frac{-G_{11}Load_3Ctrl_3-1}{\left(G_2 + \left(\frac{G_6}{-ctrl_2} \right) \right) Load_3Ctrl_3}, \quad b = \frac{-G_4Load_3Ctrl_3}{\left(G_2 + \left(\frac{G_6}{-ctrl_2} \right) \right) Load_3Ctrl_3}, \\
c &= \frac{\left(G_2 + \left(\frac{G_6}{-ctrl_2} \right) \right) Load_3Ctrl_3}{-G_{11}Load_3Ctrl_3-1}, \quad d = \frac{G_4Load_3Ctrl_3}{-G_{11}Load_3Ctrl_3-1}, \\
e &= -G_1Load_2Ctrl_2 - 1, \quad f = -G_3Load_2Ctrl_2, \\
g &= - \left(G_{12} + \left(\frac{G_5}{-ctrl_3} \right) \right) Load_2Ctrl_2
\end{aligned} \tag{3.7}$$

where $Ctrl_2$, $Ctrl_3$, $Load_2$ and $Load_3$ are the transfer functions of controllers and loads in Fig. 5. By considering the input capacitance C_1 , the input impedance of TAB converter at Port 1 is calculated as

$$Z_i = \frac{1}{Y_i + sC_1} = \frac{1}{\frac{-(f+gd)}{e+cg} \left(G_9 + \left(\frac{G_7}{-ctrl_2} \right) \right) + \frac{-(f+be)}{ae+g} \left(G_{10} + \left(\frac{G_8}{-ctrl_3} \right) \right) + sC_1} \tag{3.8}$$

IV. SPECIFICATIONS

As the structure of TAB converter has been already aforementioned in Section II and according to the requirement of MEA, the feasible parameters are listed in Table 1.

Parameter	Value	Parameter	Value
V_1, V_2, V_3	270 V	K_{p2}, K_{p3}	0.01
C_1, C_2, C_3	0.34 mF	K_{i2}, K_{i3}	1
L_1, L_2, L_3	20 uH	d_{21}, d_{31}	-0.2 → 0.2
f_s	50 kHz	R_{Load2}	37.5 ohm → ∞
R_s	0.1 ohm	R_{Load3}	37.5 ohm → ∞
$n_1:n_2:n_3$	1:1:1	The value of R_{Load2} and R_{Load3} depends on phase shift	

Table 1. Specifications of TAB converter

By employing the parameters above, the structure of TAB converter is designed to be symmetrical and it will facilitate the calculation and observation of power flow inside the converter. Besides, since the converter will be unstable if the phase shift ratio goes out the nearly linear operating region of power (-0.5, 0.5), d_{21} and d_{31} are limited in (0.2, 0.2), which not only guarantees d_{21} and d_{31} are nearly linear with power, but also indirectly makes d_{23} settle in (-0.4, 0.4), which is still in the nearly linear operating region of power.

V. THE CHARACTERISTIC OF INPUT IMPEDANCE OF TAB CONVERTER

In this section, Matlab is used to plot the characteristic of input impedance of TAB converter and PLECS is used to validate the characteristic. In addition, both symmetrical and asymmetrical power flow mode of TAB converter are investigated to see the influence on the input impedance of TAB converter.

A. Matlab plot

The characteristic of input impedance with both symmetrical and asymmetrical power flow mode is presented in Fig. 6 below:

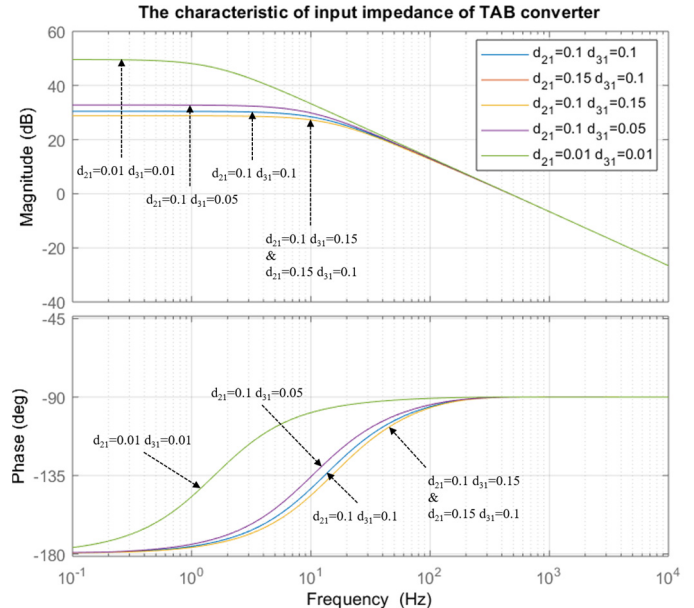
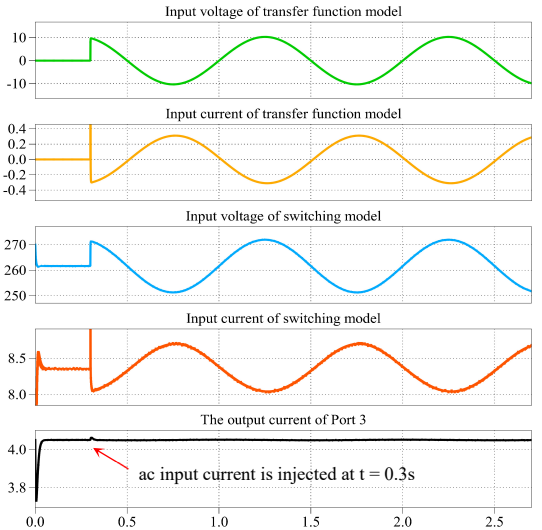


Fig. 6. The characteristic of input impedance of TAB converter

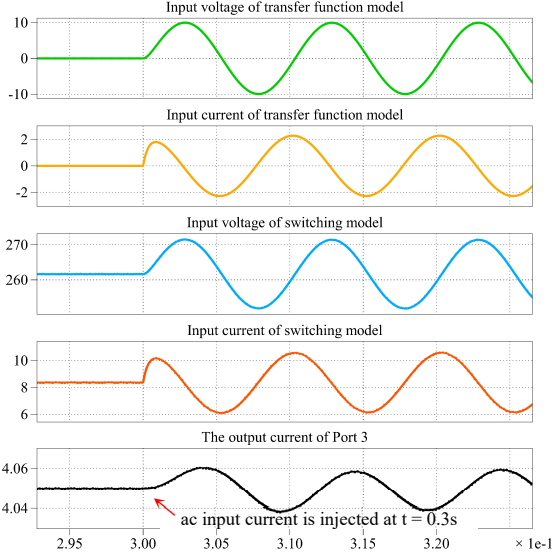
As shown in Fig. 6, in both symmetrical and asymmetrical power flow modes, the input impedance of TAB converter behaves as constant power load (CPL) at low frequencies and behaves as capacitor at high frequencies, which is same as the characteristic of input impedance of DAB converter. Moreover, it is obvious that the port power P_1 which is transferred to Port 2 and Port 3 will influence the input impedance at low frequencies. To be more specific, the lower the P_1 , the higher the input impedance at low frequencies.

B. PLECS validation

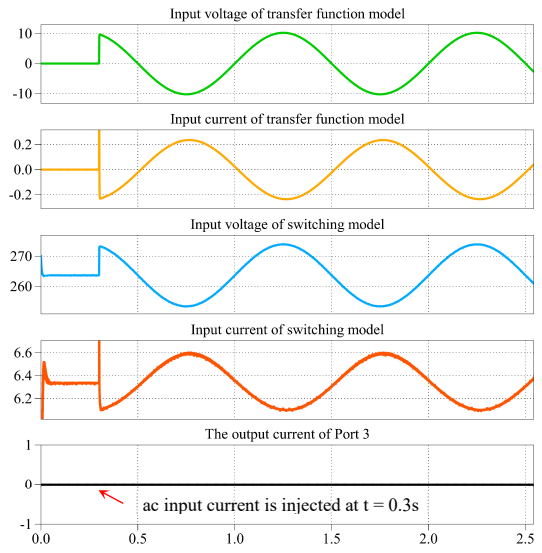
A switching model and a transfer function model are established in PLECS to validate the bode diagram shown in Fig. 6. The methodology is to inject sinusoidal ac current with different frequencies at the input port and observe the variations in input voltage. To make the sinusoidal waveforms more visible, the source resistance R_s is increased to 1 Ω. Although this change will cause a drop of input voltage, it does not influence the input impedance of TAB converter. Since it will be a huge work if validating all cases shown by Fig. 6, two of them are chosen to validate the input impedance at 1 Hz and 100 Hz in which power flows symmetrically and asymmetrically: Case 1: $d_{21} = d_{31} = 0.1$ and Case 2: $d_{21} = 0.1, d_{31} = 0.05$.



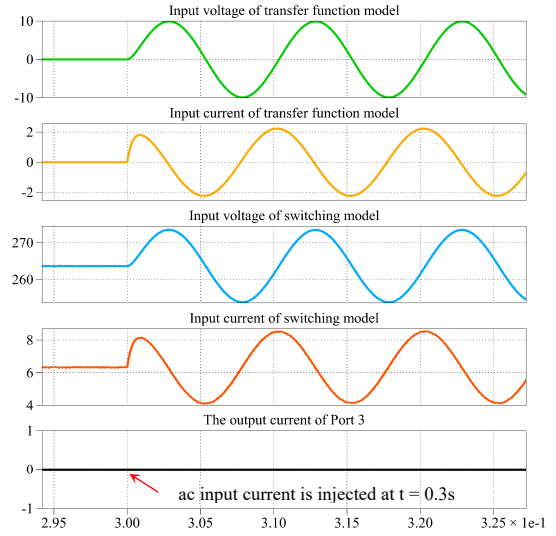
(a) Symmetrical power flow: $d_{21} = d_{31} = 0.1$ with 1 Hz ac input current



(b) Symmetrical power flow: $d_{21} = d_{31} = 0.1$ with 100 Hz ac input current



(c) Asymmetrical power flow: $d_{21} = 0.1$, $d_{31} = 0.05$ with 1 Hz ac input current



(d) Asymmetrical power flow: $d_{21} = 0.1$, $d_{31} = 0.05$ with 100 Hz ac input current

Fig. 7. Input voltage, input current of both transfer function model and switching model and the output current of Port 3

In Fig. 7, the input impedance in both symmetrical and asymmetrical power flow modes are tested. In symmetrical power flow mode, the resistance of two resistive loads at Port 2 and Port 3 are set to be same to ensure the same power flow. As for asymmetrical power flow mode, the resistive load at Port 3 is disconnected. The magnitude of input impedance at specific frequency can be calculated as

$$Z_i = \frac{V_i(\text{peak-to-peak})}{I_i(\text{peak-to-peak})} \quad (5.1)$$

By observing the waveforms of Fig. 7, the input impedance of (a) has magnitude of approximately 30.4 dB with -180° phase, the input impedance of (c) has magnitude of approximately 32 dB with -180° phase, the input impedance of (b) and (d) has lower magnitude of approximately 12.9 dB with -90° phase. Hence, all input impedance values calculated are almost consistent with the curves in Fig. 6. It proves that the transfer function based small signal model is correct.

VI. EXPERIMENTAL RESULTS

This section gives the experimental setup and preliminary experimental results. The experimental prototype of TAB converter is shown in Fig. 8, which is actually a QAB converter with one port disconnected.

During the experiment, both symmetrical and asymmetrical cases are implemented. As for experimental specifications, the input voltage and output voltage are chosen to be 60 V, the switching frequency is chosen to be 10 kHz, the control parameter K_i is chosen to be 10, other parameters are kept being same as simulation. In symmetrical case, the resistance of both loads is set to be $44\ \Omega$ to achieve the same power flow from source port to load ports. In asymmetrical case, one load is disconnected. By injecting 5 V ac voltage with different frequencies at source port, the input current will fluctuate with different amplitude. The preliminary experimental measurements of input impedance are presented in Table 2.

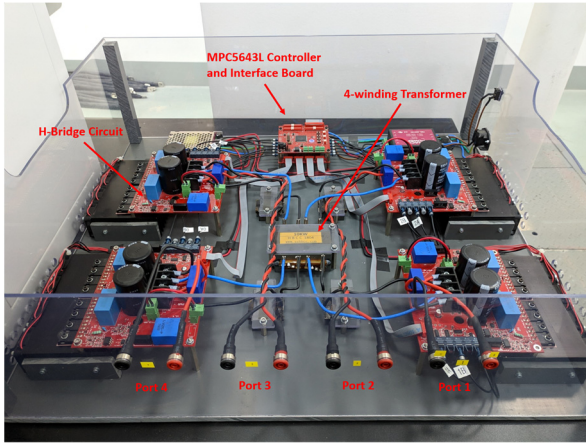
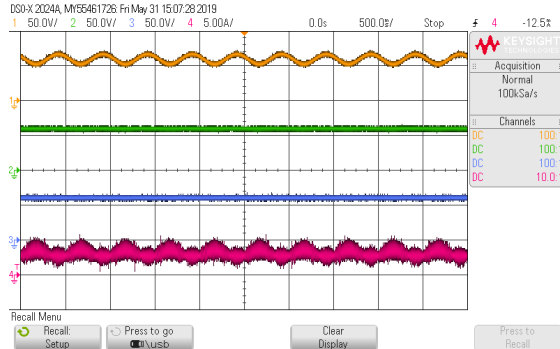


Fig. 8. Experimental prototype of TAB converter

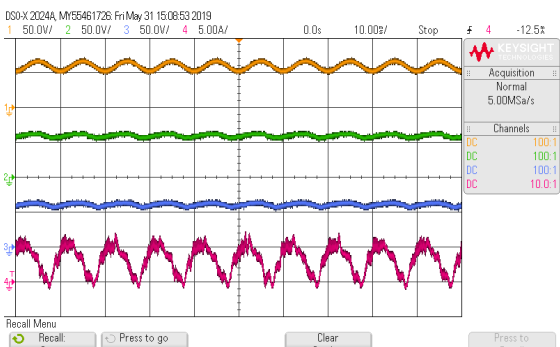
	Symmetrical case		Asymmetrical case	
Frequency	Amplitude	phase	Amplitude	phase
2 Hz	19.58	-169.9°	30.83	-167°
5 Hz	19.35	-172.6°	34.36	-151.9°
10 Hz	15.21	-169.3°	29.37	-141.9°
60 Hz	5.601	-122.5°	5.714	-114.3°
100 Hz	3.039	-109.7°	3.031	-110.7°

Table 2. Preliminary experimental measurements of input impedance

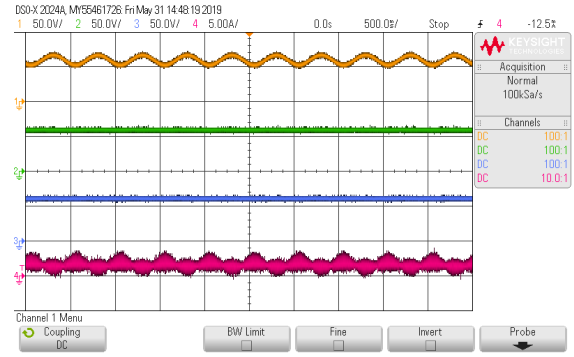
The captures of key waveforms at 2 Hz and 100 Hz in symmetrical case and asymmetrical case are shown below:



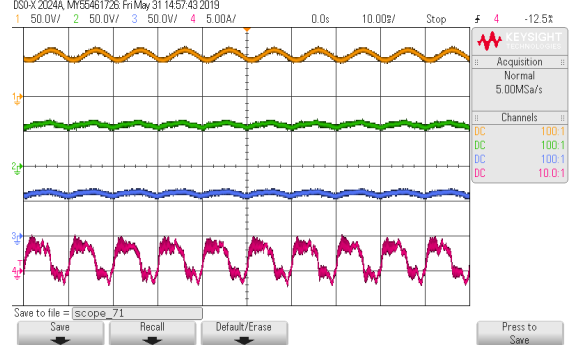
(a) Symmetrical power flow: 2 Hz ac component at input port



(b) Symmetrical power flow: 100 Hz ac component at input port



(c) Asymmetrical power flow: 2 Hz ac component at input port



(d) Asymmetrical power flow: 100 Hz ac component at input port

Fig. 9. Experimental captures of TAB converter

In Fig. 9, Channel 1 is the input voltage, Channel 4 is the input current, Channel 2 and Channel 3 are the output voltage.

By observing measured data and captured waveforms, it can be concluded that the input impedance is almost complying with the curve in Fig. 6. Furthermore, the amplitude of input impedance in the range from 2 Hz to 10 Hz in asymmetrical case is much larger than it in symmetrical case.

VII. CONCLUSION

A transfer function based small signal model is proposed to determine the input impedance of TAB converter with both symmetrical and asymmetrical power flow modes in this paper. The delta model of transformer is adopted to calculate the real leakage inductance between any two ports in TAB converter. By considering the equations of both individual power and total power, a set of small signal equations can be obtained to link the plants and controllers, hence a block scheme of small signal model is established. By using Matlab, the bode diagram of input impedance of TAB converter is plotted, which shows that the input impedance behaves as CPL at low frequencies and behaves as capacitor at high frequencies. Moreover, the output power from source will influence the input impedance, the lower the output power of source, the higher the magnitude of input impedance at low frequencies. To validate the bode diagram of input impedance, both simulation and preliminary experiments are carried out. As for simulation, a transfer function model is constructed to compare with a switching model in PLECS. By injecting sinusoidal ac current with different frequencies at input port, the input voltage of both models fluctuates equally. Similarly, in experiment the input

impedance is measured, proving the authenticity of this transfer function based small signal model.

ACKNOWLEDGMENT

This work was supported by the Ningbo Science & Technology Beauro under Grant 2017D10031, Grant 2018A610146 and the National Natural Science Foundation of China under Grant 51807099.

REFERENCES

- [1] J. S. Cloyd, "Status of the United States Air Force's More Electric Aircraft initiative," *IEEE Aerospace and Electronic Systems Magazine*, vol. 13, no. 4, pp. 17–22, Apr. 1998.
- [2] R. I. Jones, "The More Electric Aircraft: the past and the future?," in *IEE Colloquium on Electrical Machines and Systems for the More Electric Aircraft (Ref. No. 1999/180)*, 1999, pp. 1/1-1/4.
- [3] J. A. Rosero, J. A. Ortega, E. Aldabas, and L. Romeral, "Moving towards a more electric aircraft," *IEEE Aerospace and Electronic Systems Magazine*, vol. 22, no. 3, pp. 3–9, Mar. 2007.
- [4] B. Sarlioglu and C. T. Morris, "More Electric Aircraft: Review, Challenges, and Opportunities for Commercial Transport Aircraft," *IEEE Transactions on Transportation Electrification*, vol. 1, no. 1, pp. 54–64, Jun. 2015.
- [5] G. Buticchi, L. Costa, and M. Liserre, "Improving System Efficiency for the More Electric Aircraft: A Look at dc/dc Converters for the Avionic Onboard dc Microgrid," *IEEE Industrial Electronics Magazine*, vol. 11, no. 3, pp. 26–36, Sep. 2017.
- [6] P. Wheeler and S. Bozhko, "The More Electric Aircraft: Technology and challenges.," *IEEE Electrification Magazine*, vol. 2, no. 4, pp. 6–12, Dec. 2014.
- [7] D. Salomonsson and A. Sannino, "Low-Voltage DC Distribution System for Commercial Power Systems With Sensitive Electronic Loads," *IEEE Transactions on Power Delivery*, vol. 22, no. 3, pp. 1620–1627, Jul. 2007.
- [8] H. Tao, A. Kotsopoulos, J. L. Duarte, and M. A. M. Hendrix, "Family of multiport bidirectional DC-DC converters," *IEE Proceedings - Electric Power Applications*, vol. 153, no. 3, pp. 451–458, May 2006.
- [9] J. M. Guerrero, J. C. Vasquez, J. Matas, L. G. de Vicuna, and M. Castilla, "Hierarchical Control of Droop-Controlled AC and DC Microgrids—A General Approach Toward Standardization," *IEEE Transactions on Industrial Electronics*, vol. 58, no. 1, pp. 158–172, Jan. 2011.
- [10] G. Buticchi, S. Bozhko, M. Liserre, P. Wheeler, and K. Al-Haddad, "On-Board Microgrids for the More Electric Aircraft—Technology Review," *IEEE Transactions on Industrial Electronics*, vol. 66, no. 7, pp. 5588–5599, Jul. 2019.
- [11] J. L. Duarte, M. Hendrix, and M. G. Simoes, "Three-Port Bidirectional Converter for Hybrid Fuel Cell Systems," *IEEE Transactions on Power Electronics*, vol. 22, no. 2, pp. 480–487, Mar. 2007.
- [12] G. Buticchi, L. F. Costa, D. Barater, M. Liserre, and E. D. Amarillo, "A Quadruple Active Bridge Converter for the Storage Integration on the More Electric Aircraft," *IEEE Transactions on Power Electronics*, vol. 33, no. 9, pp. 8174–8186, Sep. 2018.
- [13] R. W. Erikson and D. Maksimovic, *Fundamentals of power electronics*, 2nd ed. Norwell, Mass.: Kluwer Academic, 2001.